Nanoscale

REVIEW

View Article Online
View Journal | View Issue

Cite this: *Nanoscale*, 2022, **14**, 11909

Silver based photocatalysts in emerging applications

Yan Zhang,[a] Jian Liu,[b] Young Soo Kang[c] and Xiao Li Zhang *[a]

Received 14th May 2022,
Accepted 27th July 2022

DOI: 10.1039/d2nr02665a

rsc.li/nanoscale

The infinite availability of solar energy grants the potential of fulfilling the energy demands and environmental sustainability requirements with more feasible and reliant renewable energy forms through photocatalysis. In the past decade, the intensive plasmonic effect, suitable work function, superior electrical conductivity and physiochemical properties have made Ag-based photocatalysts attractive components for emerging applications. The local surface plasmon resonance effect (LSPR) provides extra hot-carriers to participate in the photocatalytic process, and Schottky/Ohmic contacts would facilitate charge transfer. Here, recent studies focused on Ag-based photocatalysts for emerging applications are reviewed. Notably, the mechanisms of LSPR, the Schottky barrier and ohmic contacts are introduced together with urgent issues in CO_2 reduction, antibacterial application, H_2 generation, and environmental hazard removal. Additionally, some perspectives and directions on more comprehensive designs on material system, band alignment and functionalization are given to further the exploration in this research area.

1. Introduction

Sunlight, the greatest available clean free energy, allows producing chemical and electrical energies for mankind through solar-to-chemical conversion by artificial photosynthesis that mimics natural plants.[1–5] However, the recombination of photo-generated electrons and holes is generally ten times

[a]*School of Materials Science and Engineering, Zhengzhou University, 450001 Zhengzhou, P.R. China. E-mail: xiaolizhang.z@gmail.com*
[b]*Department of Chemical and Process Engineering, University of Surrey, GU2 7XH, UK*
[c]*Environmental and Climate Technology, Korea Institute of Energy Technology (KENTECH), 200 Hyeoksin-ro, Naju City, Jeollanamdo 58330, Korea*

Yan Zhang

Yan Zhang received a B.S. Degree in Measurement and Control Technology from Chengdu University of Technology, China. He is currently pursuing his M.S. Degree and working on high performance heterogeneous photocatalysis systems at the School of Materials Science and Engineering, Zhengzhou University, China, under the co-supervision of Professor Xiao Li Zhang and Professor Jian Liu.

Jian Liu

Jian Liu received his PhD degree in physical chemistry from the Dalian Institute of Chemical Physics, Chinese Academy of Science, China, in 2008, and worked at the Australian Institute for Bioengineering and Nanotechnology (AIBN), University of Queensland (UQ), as a research fellow. After working at Curtin University as a senior lecturer from 2013 to 2017, he joined DICP as a full professor and group leader of micro–nanoreactor and reaction engineering. He also held an adjunct Reader position in the Department of Chemical and Process Engineering, University of Surrey, UK. His research focuses on the design of micro–nanoreactors, porous carbon spheres, and industrialization of homogeneous catalysis in heterogeneous systems. His h-index is 58, and he was listed as a 2018/2019/2020 Highly Cited Researcher (Clarivate Analytics).

faster than the transfer from the body phase to the surface of the photocatalyst, which significantly suppresses the photosynthesis ability.[6,7] Moreover, Earth-abundant and environmentally benign semiconductors such as TiO_2 and ZnO are particularly wide bandgap semiconductors, which can only utilize the ultraviolet range of the solar spectrum (merely 5%).[8–10] Thus, broadening the photoactive spectrum region and prompting charge transfer while retarding recombination are urgent needs for the development of highly efficient and stable photocatalyst systems.[11–13]

Silver, a typical plasmonic metal, possesses adjustable intensive LSPR through control over size, shape, temperature, and irradiation intensity.[14–17] Induced by visible light, the LSPR effect is able to generate extra electrons and holes to participate in the photocatalysis. Meanwhile, the suitable work function allows Ag to establish efficient charge separation between the semiconductor and Ag through the construction of a Schottky junction or Ohmic contact within the metal–semiconductor structure.[18,19] The multiple roles of Ag – hot carrier provider, visible light response inducer and electron trapper – effectively enable a broad photoactive spectrum region and rapid charge transfer while hindering the recombination.[3,20,21] As illustrated in Fig. 1, a number of Ag based photocatalysts were explored for diverse applications such as CO_2 reduction, antibacterial application, water splitting, pollutant removal, *etc*. Meanwhile, a list of critical issues awaiting suitable solutions were summarized: the low selectivity towards liquid fuels such as alcohol and other hydrocarbons in the photocatalytic CO_2 reduction process on Ag based photocatalysts, the slow oxygen evolution kinetics during water splitting, how to control equably Ag^+ release within a long period, and low charge separation efficiency during pollutant degradation.

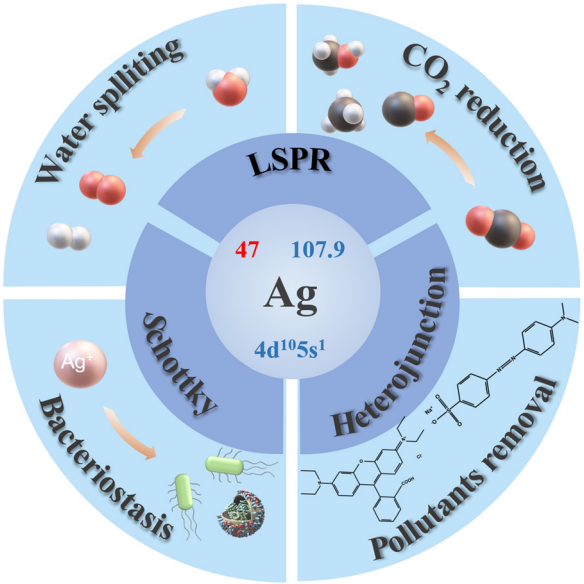

Fig. 1 Photocatalytic applications of Ag based photocatalysts (gray: hydrogen atom; black: carbon atom; pink: oxygen atom).

The aforementioned superior properties of Ag metal have attracted great research interest as leverage strategies for the development of photocatalysis systems with better performance, which was demonstrated by several excellent reviews. For example, Sharma *et al.* summarized the synthesis and electro- and photo-catalytic applications of Ag nanoparticles and Ag based nanomaterials.[22] Zhu *et al.* reviewed the catalytic applications of atomic noble metal nanoparticles.[23] A review article from Haynes *et al.* focused on the stabilization strategies for

Young Soo Kang

Young Soo Kang is a Professor at the Environmental and Climate Technology, Korean Institute of Energy Technology (LENTECH), Naju, Jeollanamdo, Korea. He has worked as a review panel member for ACS, Wiley Science and Elsevier chemistry journals. He received a BSc and MSc degree in Chemistry from Pusan National University, Busan, Korea in 1984 and 1986 and Ph.D. degree from the University of Houston, U.S.A in 1992 and a postdoctoral fellowship at the University of California at Berkeley and Stanford University, respectively, for his work on Nanomaterials and Surfactant Related Materials Chemistry. Current research interests are focused on the synthesis and application of nanostructured materials in the IT and energy related fields. He has published over 170 articles in journals from ACS, Wiley Science and Elsevier.

Xiao Li Zhang

Xiao Li Zhang received her B.Sc. degree (2001) in Chemistry from Shandong University, China. Upon completing her PhD (2008) in Materials Chemistry under Prof. Young Soo Kang at Pukyong National University, Korea, she worked as a Research Fellow (2008–2011) with Prof. Yi-Bing Cheng and Prof. Udo Bach at Monash University, Australia. After a short stay at the University of Melbourne, Australia, she commenced her VC Fellowship (2012) at the University of New South Wales, Australia, working with Prof. Rose Amal. Then she worked with Prof. Zheng Xiao Guo at the University College London, UK, before taking a full professor position at the Zhengzhou University, China. Her current research focuses on the construction of mesoporous and heterogeneous catalysts for solar energy conversion.

plasmonic Ag nanoparticles.[24] Chen *et al.* worked on reviewing the application of Ag as a co-catalyst in selective CO_2 photoreduction.[25] Plasmonic properties and applications of Ag nano porous metal were summarized by Garoli *et al.*[26] Overall the relative reviews focused on very specific categories, *e.g.* plasmon-enhanced organic transformation by silver-based catalysts,[27] nano-Ag coated surfaces for photocatalytic bacterial inactivation,[28] visible light driven water disinfection on silver/silver halide constructed photocatalysts,[29] Ag–semiconductor based Z-scheme photocatalytic systems,[30] *etc.*, while an overview of the comprehensive nature and photocatalysis applications of Ag based photocatalysts is still missing. The use of one type of charge transfer mechanism is unlikely to overcome the current limits, while dedicated design of the photocatalyst system with well aligned multiple functions might enable a synergistic solution to strengthen the overall photocatalytic performance. Here, based on the fundamentals of the LSPR, Schottky junction and ohmic contact within Ag based photocatalysts, we reviewed the emerging photocatalytic applications and issues in CO_2 reduction, antibacterial application, pollutant degradation, water splitting with some proposed perspectives and directions in this field at last.[31]

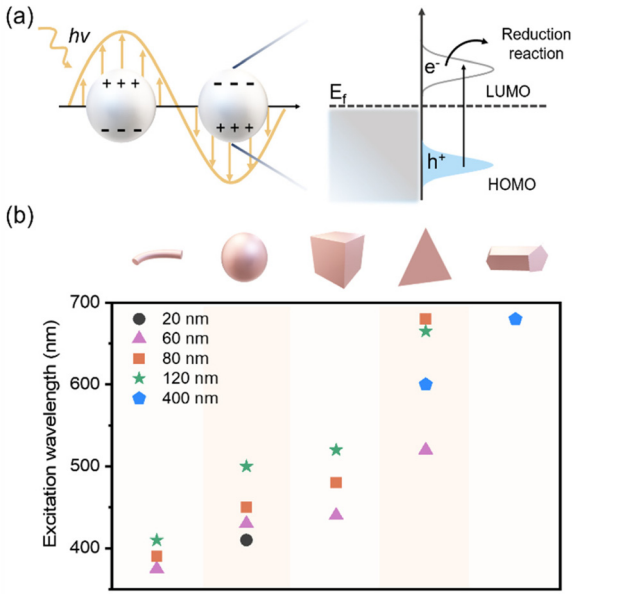

Fig. 2 (a) The mechanism of the LSPR effect within Ag nanoparticles. (b) Plasmon excitation peaks of different Ag morphologies and sizes, the "size" represents the diameter of sections (nanowire/penta-twinned crystalline nanowires, nanosphere and nanoprism), diameter and length of sides of nanocubes, respectively.

2. Metallic silver

Metallic Ag allows morphological surface modification, localized spatial charge separation, and rapid charge separation and trapping in the participated heterogeneous systems that greatly benefit the photocatalytic performance. In general, the LSPR effect and the Schottky effect are the two principal roles of metallic Ag in the enhancement of photocatalysis. The following section will focus on summarizing the corresponding mechanisms and the associated heterogeneous photocatalyst systems with emerging applications.

2.1 LSPR effect of silver

The LSPR effect was firstly observed by Wood in 1902 and refers to the coinstantaneous coherent oscillation of all electrons induced by the incident photons of equal frequency to the natural oscillation frequency of electrons on the surface of plasmonic nanoparticles (NPs) (Fig. 2a).[32–35] Along with the collective oscillation of electrons, a local electromagnetic field also forms on the surface of the plasmonic NPs. The following relaxation decay is through radiative or non-radiative damping. The non-radiative damping enables the generation of hot electrons and holes that can participate in the chemical reaction.[36–38]

To date, the most studied plasmon metals, Au and Ag, both possess intensive LSPR effects. Benefiting from the cheaper price and tuneable LSPR, Ag was broadly utilized in many photocatalytic systems aiming at effective light harvesting and efficient energy conversion at the visible region. For example, Lee *et al.* demonstrated direct evidence for the tuneable LSPR effect of Ag.[39] They found that Ag NPs with the size of 25 nm exhibited the strongest LSPR phenomenon and the highest activity in the degradation of aqueous salicylic acid and aniline. The geometric and size correlated LSPR was reflected by the different excitation wavelength of Ag nanowires, nanospheres, nanocubes, nanoprisms and penta-twined crystalline nanowires of varying sizes/diameters (Fig. 2b).[40–49] According to the research from Lei *et al.*, the dipole and quadrupole resonance modes of pure Ag NP arrays occurred at ~480 and 350 nm, respectively.[50] It was also reported by Lei and coworkers that adjusting the thickness of the surface coating of the LSPR nanoparticle allowed fine-tuning the dipole resonance frequency. When continuously adjusting the thickness of TiO_2 from 5 nm to 40 nm, the dipole resonance frequency of Ag@TiO_2 gradually red-shifted from ~510 to ~575 nm with the strongest LSPR localized at approximately 565 nm for a TiO_2 thickness of 25 nm. Mirkin *et al.* sulfurized Ag nanoprisms with Na_2S_x and obtained Ag/Ag_2S core/anisotropic shell structures.[43] In this work, the existence of Ag_2S significantly influenced the dipole plasmon mode of Ag. Tuning the radial ratios of Ag_2S and Ag in the Ag/Ag_2S core/shell structures enabled progressive blue- or red-shift of the dipole plasmon mode of Ag. Extending the phenomena to other plasmonic metal–semiconductor nanostructures might open new paths for delicate modification of rational morphologies and LSPR effect. The tuneable LSPR of Ag across a wide range of wavelength and even reaching to visible light offers great opportunity to utilize hot carriers to induce chemical reaction in the visible light range in a more efficient manner.[36] Thus, coupling Ag with acceptor species, such as semiconductors, carbon-based materials and other metals, was explored.[51]

Modifying Ag with traditional catalysts, such as TiO_2, g-C_3N_4, MoS_2, and BiOCl, can prolong charge lifetime due to

the efficient carrier transfer between Ag and semiconductors.[52–55] In the meantime, the LSPR effect of Ag can enable visible light harvest for photocatalytic systems and reduce the activation energy barrier for chemical reactions.[10] In recent years, tremendous exploration has been concentrated on TiO_2, one of the excellent candidates that has been studied comprehensively in photocatalytic applications. For example, Wang and co-workers successfully synthesized the closely contacted plasmonic Ag–TiO_{2-x} nanocomposites through a simple photochemical reduction with post-annealing.[56] Benefiting from the LSPR effect of Ag, the Ag–TiO_{2-x} nanocomposites exhibited approximately twice of the NO removal rate under visible light irradiation ($\lambda > 420$ nm) than that of the pure commercial P25 TiO_2. Lin *et al.* developed a mussel-inspired strategy to prepare Ag-decorated ultra-thin g-C_3N_4 nanosheets, which served as Ag@U-g-C_3N_4-NS.[53] The combined strong SPR of Ag and the large surface area of U-g-C_3N_4-NS resulted in an excellent degradation activity towards methylene blue (MB) and phenol removal. In general, the stable photocatalytic activity originates from a long lifetime of the charges. The extreme stable degradation rate for MB and phenol was due to the efficient charge separation between Ag NPs and U-g-C_3N_4-NS. The perovskite semiconductor of $CsPbBr_3$ was chosen to support Ag nanoparticles by Zhang *et al.*[57] Due to the significantly increased the metal–semiconductor coupling by the strong oscillation strength of $CsPbBr_3$ inter-band transition, the plasmon-induced transfers of the hot electrons and the resonant energy were successfully observed under the time scale of <100 fs.[57] This finding opens a novel approach for efficient plasmon-induced hot electron devices through strategically utilizing perovskite semiconductors as an excellent hot electron and energy transfer material.

In addition, coupling Ag with charge-affinity carbon-based materials, such as carbon fibres, graphene and many others, is also an effective approach to separate the photon-induced charges.[58,59] Carbon-based materials of porous structure and large surface area are particularly explored to gain better catalytic performance. An *in situ* growth of graphene on the Ag NP surface using C_2H_4 as the precursor was reported by Zhang *et al.*[60] The corresponding *in situ* surface-enhanced Raman scattering (SERS) revealed D and G bands of graphenic carbon at ~1340 and 1570 cm^{-1}, and 2D mode, D + G mode and 2G mode at 2650 cm^{-1}, 2890 cm^{-1} and 3160 cm^{-1}, respectively, which confirmed the formation of graphenic carbon. More importantly, the ethylene oxide and CO_2 species from C_2H_4 epoxidation only emerged when graphene carbon was observed on the surface of Ag, demonstrating that the coupled Ag plasmonic NPs and the graphenic carbon composite was the active phase for the C_2H_4 epoxidation. Pichiah *et al.* observed higher activity from the GO–Ag–TiO_2 nanotubes (GO–Ag–TNTs) on photodegradation of MB and 2-chlorophenol (2-CP) than the GO–TNTs.[61] The prior deposited Ag nanoparticles acted as a charge transfer mediator between the TNTs and GO that solved the charge transfer issue in the previous GO–TNTs system. The prompted charge separation/transfer greatly contributed to the photocatalytic activity.

2.2 Schottky and ohmic contacts

Schottky and ohmic contacts exist at the interfacial area of the intimately contacted metal and semiconductor. The energy level variance between the Fermi level (E_F) of the semiconductor and metal drives the electron flow from the higher one toward the lower one. In the case of the Schottky junction (Fig. 3a), electrons will continually transfer to metal with lower E_F (higher work function) from the semiconductor, which results in the development of an internal electric field (IEF) pointing in the direction from the semiconductor to the metal that inhibits further electrons flow.[62] In another word, the Fermi levels of semiconductors and metal become equal along with the formation of the Schottky barrier. Due to the upward band bending towards metal, the Schottky junction easily directs the flow of photo-generated electrons from the metal to semiconductor. In contrast, during the formation of the ohmic junction, the occurrence of a contrary electron flow leads to the opposite IEF (Fig. 3b), which drives electron flow to the opposite direction (the metal). Take water splitting as an example, ohmic contact benefits the transfer of photo-excited electrons to metal co-catalyst to participate H_2 evolution, whereas electrons are hard to arrive at the metal through the Schottky junction until adequate H* on metal reduces the barrier height. In another half-reaction of O_2 evolution, the Schottky junction can efficiently separate the photo-generated electrons to the semiconductor and thus facilitate the O_2 evolution on metal, which is difficult for ohmic contact.[63,64] In a practical photocatalytic system, the transfer pathway of photo-generated electrons can be feasibly guided through construct-

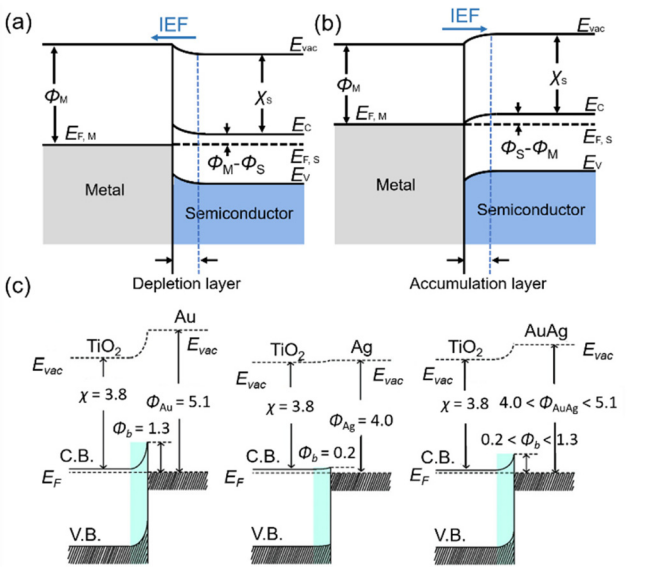

Fig. 3 (a–b) Schematic illustrations of the Schottky junction (a) and ohmic contact (b); E_{vac}: vacuum energy level; E_C: conduction band; E_V: valence band; $E_{F,s}$: Fermi level of semiconductor; $E_{F,m}$: Fermi level of metal; Φ_m: work function of metal; Φ_s: work function of semiconductor; X_s: electron affinity of the semiconductor. (c) The band structures of Au/TiO_2, Ag/TiO_2 and AgAu/TiO_2. (c) Reproduced with permission from ref. 67 Copyright (2012) American Chemical Society.

ing Schottky or ohmic contacts and adjusting barrier height. The medium work function of Ag enables high feasibility to achieve the goal mentioned above.

Dual functionalized by the LSPR effect and the Schottky junction between Ag and the semiconductor, the charge carrier separation efficiency of the Ag/semiconductor system would be significantly improved and lead to a great photocatalytic activity enhancement. For instance, Ag can accept photo-generated electrons from conventional junctions. Shen *et al.* prepared ternary porous hollow Ag/ZnO/$ZnFe_2O_4$ composites which involve a conventional type-II junction at the interface between ZnO and $ZnFe_2O_4$ and a Schottky junction at the Ag/ZnO interface.[65] During the catalytic reaction, the cooperation of type II junction and Schottky junction enabled efficient electron transfer with Ag as an excellent trapper for the photo-excited electrons while adsorbing enough oxygen on it. Shi and co-workers developed a ternary CQDs/Ag/Ag_2O for the photocatalytic elimination of pollutants, relying on the Schottky junction in the stack structure of the noble metal/CQDs/semiconductor.[66] The CQDs were prepared through an alkali-assisted ultrasonic deposition on the Ag_2O through the reaction between $AgNO_3$ and $NH_4H_2PO_4$. Further reduction using $NaBH_4$ enabled the formation of CQDs/Ag/Ag_2O, which exhibited significantly enhanced MB degradation rate in the region from visible light to NIR light. The noteworthy photocatalytic performances originated from the cooperated Schottky barrier effect at the Ag/ZnO interface, SPR effect of Ag and electron mediator CQDs. Lei *et al.* synthesized Ag–Ag_2S/$BaTiO_3$ through a simple deposition–precipitation process involving the deposition of Ag nanoparticles *via* a light-reduction reaction and the subsequent high temperature reaction of Ag particles with sulphur powder for Ag_2S.[15] Compared to pure $BaTiO_3$, the greatly enhanced photocatalytic performance of the Ag_2S/$BaTiO_3$ heterojunction possessed dual-function from the piezoelectric polarization and the synergistic exciton–plasmon interaction in Ag–Ag_2S. Facilitated by the exciton–plasmon interaction, the enhanced LSPR effect could significantly improve the hot electron generation on the Ag and charge transfer through the Schottky junction energy barrier to the $BaTiO_3$. Additionally, the piezoelectric effect of $BaTiO_3$ could induce a built-in piezoelectric field that decreased the energy barrier of Ag/$BaTiO_3$ Schottky junction and adjust the band alignment of Ag_2S and $BaTiO_3$ from type I to type II leading to higher photon absorption and more efficient charge separation.

The Schottky junction energy barrier height (Φ_{SB}) can be estimated using the formula $\Phi_{SB} = \Phi - \chi$, in which Φ denotes the work function of the metal (or alloy), and χ represents the electron affinity for the CB of the semiconductor. Metal of higher work function can form a higher Schottky junction energy barrier with the same semiconductor as those of lower Φ, reflecting the stronger electron capture ability of the metal and greater reduction ability for the electrons that cross the energy barrier. However, an extremely high Schottky junction energy barrier would significantly limit the crossing over of electrons, in particular, those of low energy. Bimetallic alloy structures have therefore been fabricated to obtain tuneable work function and barrier height to optimize photocatalytic activity.

Au, Pt and Pd are usually coupled with Ag to further facilitate charge separation with the charge transfer direction from Ag to Au, Pt and Pd. Take Au and Ag as examples, which have a work function of ~5.1 eV and ~4.0 eV, respectively. A Schottky junction energy barrier height is 1.3 eV at the interface between TiO_2 and Au, and 0.2 eV for the TiO_2 and Ag interface. Yasuhiro *et al.* demonstrated adjustment of the Schottky junction energy barrier through constructing the AuAg/TiO_2 heterojunction, which possessed a tuneable energy barrier height from 0.2 eV to 1.5 eV (Fig. 3c).[67] In another word, the AuAg alloy provided an intermediate barrier with TiO_2 of a proper energy barrier height that allowed electrons flow from the TiO_2 to Ag then to the more electronegative Au and thus greatly prompted charge transfer efficiency. In a similar case, Haider *et al.* had an insight of the band structure modulation for noble metal alloy (Ag_xAu_{1-x}) through DFT calculations.[63] The Schottky junction energy barrier height can be adjusted by tuning the d-band of Ag_xAu_{1-x} alloy. The appropriate d-band position would realize efficient electron injection to TiO_2 with a low recombination rate. Miguel *et al.* achieved an H_2 generation rate in excess of 60 mmol h^{-1} g^{-1} using the bimetallic Au@Ag alloy nanorods which is far beyond that of the monometallic Au nanorods (less than 40 mmol h^{-1} g^{-1}) with similar geometries.[51] The limited inter-band damping effect and stronger surface plasmonic resonances in Ag boosted hot-electron injection rates leading to an excellent HER.

Yan *et al.* modified the g-C_3N_4 surface with Ag and Ni nanoparticles at different locations through precipitation and photoreduction, respectively.[68] Ni nanoparticles enriched electrons in Ni/g-C_3N_4/Ag nanocomposites through the Schottky junction which built an electric field towards the surface of g-C_3N_4, while the Ag nanoparticles served as an electron trapping site through ohmic contact with g-C_3N_4 that forms an electric field towards the inside of g-C_3N_4. This enabled rapid charge carrier transfer with the separated oxidation reaction and reduction reaction occurring on Ni and Ag, respectively. Yu and co-workers utilized a typical polyol method to couple PdAg alloy nanowires with g-C_3N_4 (PdAg NWs@g-C_3N_4) for the formic acid dehydrogenation.[69] The binding energy of Ag $3d_{3/2}$ was beyond that of Pd $3d_{3/2}$ NWs while Pd $3d_{3/2}$ has a binding energy lower than that of Pd $3d_{3/2}$ NWs, which suggested the electron transfer direction was from g-C_3N_4 and Ag to Pd due to the Mott–Schottky heterojunction in the PdAg NWs@g-C_3N_4 and thus further prompted photocatalytic performance. Weng *et al.* combined noble metal Ag/Au/Pt ternary alloy with ZnO to form metal–semiconductor heterojunctions, in which the Schottky junction was formed between Au/ZnO and Pt/ZnO while ohmic contact existed in Ag/ZnO.[70] The downward band bent of the Ohmic contact towards Ag drives the photo-generated electrons from the CB of ZnO to metallic Ag. In another instance, Huang *et al.* reported reverse electric fields (E_B) at the metal–ZnO interfaces – Ohmic contact between Ag/ZnO and the Schottky junction between Pt/ZnO, which enabled the

opposite direction of electron migration and dramatically enhanced the charge separation.[71]

Coexistence of the LSPR effect and the Schottky junction in the system of a surface plasmonic metal–semiconductor might induce competition between the hot electron migration and charge transfer driven by the Schottky barrier. To address this issue, Xiong *et al.* strategically utilized the BiOCl (001) facet of electron-affinity and (110) facet of hole-affinity to construct the BiOCl (001)–Ag (100) interface and BiOCl (110)–Pd interface that successfully implemented non-competitive charge separation.[72] The surface plasmonic deep holes on Ag were injected into the VB of BiOCl (001), then migrated through the VB of BiOCl (110) and the Schottky junction energy barrier on the BiOCl (110)–Pd interface, finally trapped by Pd. The successful physical isolation of Ag and Pd on different BiOCl facets enabled synergistic utilization of the LSPR effect and the Schottky junction energy barrier at the same time, opening a new approach to construct novel dual-functional metal–semiconductor junctions.

In summary, metallic Ag enables rapid charge separation and superior light harvest abilities to the photocatalytic systems. On the one hand, the intensive LSPR effect of metallic Ag in the visible light region can provide extra hot electrons and holes under photon excitation to further prompt the photocatalytic activity in a more broadened range of the solar spectrum. On the other hand, the Schottky junction and ohmic contact between Ag and semiconductors allow various strategic junction constructions to realize efficient charge separation and transfer through the barrier and inner electric field, respectively. Metallic Ag can be widely applied in most of the photocatalytic applications to enable visible light activity and prolong charge lifetime.

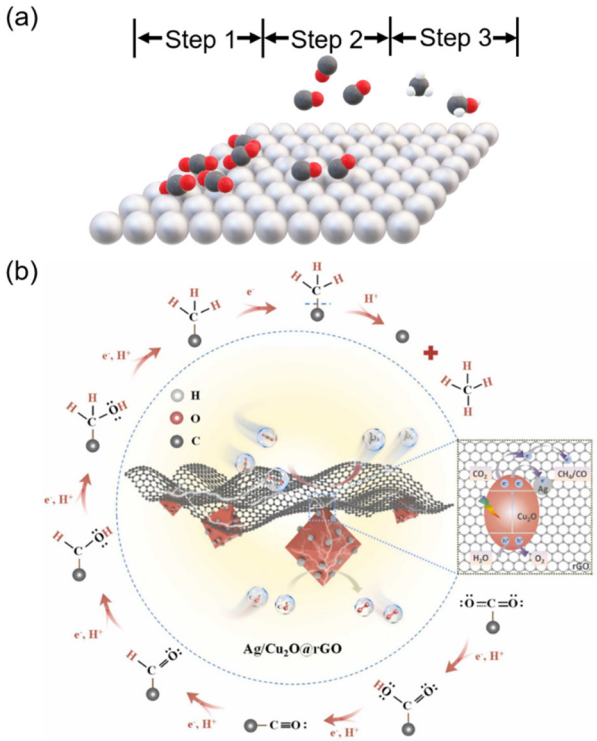

Fig. 4 (a) The photocatalytic CO_2 reduction process on Ag (gray: silver atom; black: carbon atom; white: hydrogen atom; red: oxygen atom). (b) The CO_2 reduction pathway on Ag/Cu_2O@rGO. (b) Reproduced from ref. 80, Copyright (2017), with permission from Elsevier.

3. Photocatalytic applications

3.1 CO_2 reduction

The CO_2 reduction process consists of multiple steps and multiple pathways,[73] which frequently starts from the CO_2 to CO* as the first reduction step followed by the hydrogenation process.[74,75] Ag metal exhibited extremely low selectivity towards alcohol and hydrocarbon due to the weak hydrogenation kinetic process on it. This was attributed to the high chemisorption energy of CO* on Ag metal, which hinders the binding process between CO* and H.[76] Fig. 4a depicts the corresponding processes: the initial CO_2 molecular adsorption on the surface of Ag nanoclusters or nanoparticles (step I); the subsequent reduction to CO by the photogenerated electrons and then desorption of CO as majority product due to the low adsorption energy on the Ag (step II); and further reduction of the remained CO* into alkane and alcohol hydrocarbon as minority products (step III). For example, Xiang *et al.* deposited Ag nanoparticles (NP) on layered double hydroxide (U-LDH) to enhance CO selectivity.[77] The obtained Ag@U-LDH exhibited 94.5% CO selectivity while pure U-LDH only reached ~80%, which demonstrated the high CO selectivity rather than alcohol and hydrocarbon on Ag NPs.

Take the low alcohol/hydrocarbon selectivity of Ag into account, building extra reduction sites was an effective strategy to address this issue. For instance, Zhou *et al.* co-loaded TiO_2 and Ag NP on zeolite TS-1 (TS-1) with a high surface area.[78] The selectivity towards CH_4 was raised after improving the weight of high dispersed TiO_2 nanoparticles, which well demonstrated the selectivity of Ag based photocatalysts can be tuned through adjusting the CO_2 reduction sites. Kon *et al.* designed an Ag@TiO_2 core–shell structure for CH_4 evolution from CO_2 reduction.[79] CO_2 adsorption on the TiO_2 shell enhances the CH_4 selectivity while the Ag core boosted light harvesting through the LSPR effect.

The desorption energy of the CO* intermediate on reduced graphene oxide (rGO) was 0.065 eV while the protonation of CO* was an exothermic process (−0.358 eV).[80] Based on this property of rGO, Wei and co-workers strategically coated rGO on Ag/Cu_2O to improve CH_4 selectivity. In the rGO/Ag/Cu_2O system, Ag NPs enriched photoelectrons through the LSPR effect and bridged electron transfer from Cu_2O to rGO (Fig. 4b). Meanwhile, the superior reactant/intermediate adsorption ability and steady exothermic hydrogenation process on rGO ensured the excellent CH_4 selectivity. This strategy offered a novel approach to elevate CH_4 selectivity on Ag based photocatalysts. Similarly, Fan *et al.* coupled Ag NPs

with porous carbon fibers to enhance the CH_3OH selectivity.[58] Hot electrons from Ag NPs could reduce CO_2 into CO*, while the holes left on Ag NPs would oxidize H_2O into O_2 and H*. H* would subsequently participate in the hydrogenation process inducing the high selectivity of CH_3OH.

Niu *et al.* optimized the proportion of AgBr decorated on g-C_3N_4/nitrogen-doped graphene. With an AgBr proportion of 50 wt%, the corresponding ACNNG-50 sample demonstrated excellent photocatalytic activities in both water purification and CO_2 reduction.[81] G-C_3N_4 acted as the CO_2 reduction site and led to the selectivity towards methanol and ethanol, reaching 105.89 μmol g^{-1} for methanol and 256.45 μmol g^{-1} for ethanol under visible light illumination, respectively, which demonstrated the highly selective CO_2 reduction ability of the AgBr–Ag-CN.

Apart from the construction of reduction sites, other strategies such as morphological engineering and Ag nanocluster modification were also developed. For example, Zhang and co-workers demonstrated significantly enhanced selectivity towards CH_4 of Ag/Pd bimetal alloy NPs than the single metal Ag NPs on N-doped TiO_2 under aqueous conditions,[82] which might be due to the better CO* adsorption ability of Pd.[76] Bimetallic systems exhibit a promising approach to establish tuneable selectivity of the Ag based photocatalysts. Separately, Ag clusters with a smaller size possessed a higher work function than the larger ones.[83] The band bending between Ag clusters and semiconductor could be enhanced following the reduced cluster size, which could facilitate the charge separation at the metal/semiconductor interface. For example, Jin *et al.* fabricated Ag_{25} clusters consisting of a ligand protected Ag_{12} shell and an Ag_{13} core for photocatalytic CO_2/H_2 to CH_4.[84] Photo-generated electrons in the Ag_{25} cluster system contains two aspects – plasmonic induced electrons and excitation electrons on the LUMO. The corner and edge atoms of the Ag_{12} shell have good activity towards hydrogen molecular activation. Plasmonic induced hot electrons drove the adsorbed CO_2 molecule to form $CO_2^{\bullet-}$, which was then activated by H* to generate intermediators of HCO* and H_2CO* towards the CH_x product.

3.2 Water splitting

The photocatalytic water splitting reaction is a significant process to decompose water into more valuable H_2 and O_2 (Fig. 5a), which is facing the main limitation from inefficient charge separation. The aforementioned LSPR, Schottky junction and ohmic contact enable alternative strategies to facilitate efficient charge separation and transfer. A series of Ag based catalysts were developed to upgrade the water splitting efficiency.

Wang *et al.* thoroughly studied the roles of the Ag nanocluster in the $Ag_{44}(SR)_{30}/TiO_2$ (SR = thiolate) photocatalytic system.[85] The $Ag_{44}(SR)_{30}$ cluster served as a photosensitizer under visible light irradiation when electrons on the HOMO were excited to the LUMO+1 then transfer to the CB of TiO_2, while the TiO_2 itself was inactive under visible light. In the case of using UV-vis light, as both the $Ag_{44}(SR)_{30}$ cluster and

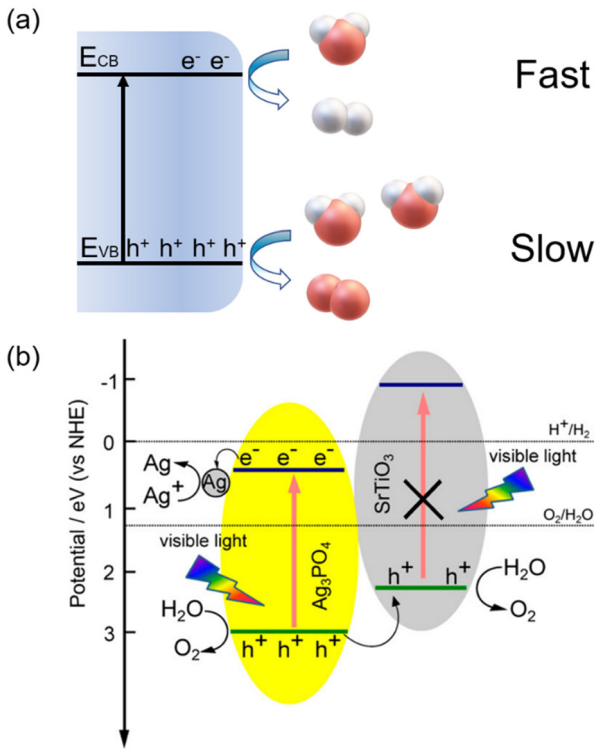

Fig. 5 (a) The comparison between HER and OER kinetics. (b) The OER mechanism within $SrTiO_3/Ag_3PO_4$. (b) Reprinted with permission from ref. 99 Copyright (2014) American Chemical Society.

TiO_2 were activated, the photo-generated holes on VB of TiO_2 migrated towards HOMO of $Ag_{44}(SR)_{30}$ to facilitate charge transfer. $Ag_{44}(SR)_{30}$ clusters acted as dual-functions for both the photosensitizer and cocatalyst to enable efficient charge separation. Hiromi and co-workers explored the plasmonic effect of the Pt/Ag bimetallic system, where Ag and Pt were deposited on the mesoporous silica through a microwave (MW) assisted alcohol reduction and plasmon-mediated deposition, respectively.[86] The final nano-catalyst was labelled Pt/Ag/SBA-15. The deposited Pt not only generated hot electron–hole pairs through the SPR effect, but also attracted electrons from Ag, facilitating the charge separation as a result of its excellent electron trapping ability. The Pt/Ag/SBA-15 revealed an intense plasmonic peak at 420 nm with an optimum H_2 production from ammonia borane (NH_3-BH_3) from the Pt (0.25)/Ag/SBA-15. Han and co-workers coated Ag nanoparticles with N, O-doped ultrathin carbon layers (denoted as Ag@N,O-C GLLS).[87] In this ginkgo-leaves-like structure, the strong anchoring effect of the Ag surface and N, O-doped carbon layer led to the development of an intimate inter-connection between the Ag nanoparticles and the N, O-doped ultrathin carbon layers as demonstrated by the DFT simulation. The N, O-doped carbon layer significantly prolonged the lifetime of the charge separated state through rapid electron capture from the Ag that enhanced the HER efficiency.

Ho *et al.* loaded Ag_2S nanoparticles on the porous TiO_2 spheres through a room temperature ionic deposition with

$AgNO_3$ and $SC(NH_2)_2$ served as a precursor for Ag^+ and S^{2-} ions.[88] Ag_2S significantly improved the visible region light absorption of the TiO_2 spheres. The $Ag_2S/CdS/Cd_2SO_4(OH)_2$ composites (*x*ACC, *x* represents the amount of $AgNO_3$ during preparation) were synthesized by Wang and co-workers to establish UV-vis-NIR photocatalytic HER activity.[89] $Cd_2SO_4(OH)_2$ was easily reduced to Cd metal by the photo-irradiation that effectively trapped the electrons during photocatalysis. Additionally, Ag_2S enabled the full spectrum adsorption of the ACC system. The 7ACC of a completed reduction of $Cd_2SO_4(OH)_2$ to Cd metal exhibited excellent HER evolution ability under UV and visible light irradiation, and even showed NIR light activity.

Anisotropic Ag_2S-edged Au-triangular nanoprisms (TNPs) as the surface plasmonic photocatalyst for H_2 generation were successfully carried out *via* a controlled prior overgrowth of Ag_2S.[90] Strong PL quenching was observed on the anisotropic Ag_2S-edged Au-TNPs that suggested SPR-induced hot electron migration from Au-TNPs to Ag_2S. Demonstrated by finite-difference-time-domain simulations, the maximum electric field distributed at the high-curvature sites of the Au-TNPs such as corners and edges. This benefited the hot electron transfer and led to a HER efficiency of 796 μmol h^{-1} g^{-1} of Ag_2S-edged Au-TNPs, nearly four-times higher than that of Ag_2S-covered Au-TNPs and pure Au-TNPs. Toshiharu *et al.* applied the Ag_2S layer as a carrier-selective blocking layer to prevent the photo-excited electron separation from CdS to Ag that contributed to the noteworthy promotion on the hole transfer in the Ag–Ag_2S–CdS system.[12] The corresponding time-resolved transient absorption spectra demonstrated that k_{r1} and k_{r2} are estimated to be 8.8 ± 0.6 and 96 ± 7 ns, indicating that the prolonged electron lifetime benefited the photocatalytic HER performance.

An ohmic junction is obtained at the interfacial area when Ag comes into contact with the ZnO, and then the photo-generated electrons on the CB of ZnO migrates to Ag under illumination. Different from the ohmic contact, the Schottky junction offers an opposite barrier direction.[91] An *et al.* developed a Schottky junction in $Ag_xAu_{1-x}/ZnIn_2S_4$ to obtain a desired barrier height.[92] At x = 0.6, the photocatalytic composite reached the highest H_2 production rate, indicating the most efficient photo-induced electron–hole separation and transfer as a result of the suitable Schottky barrier height.

The oxygen evolution reaction (OER), is the other half-reaction of the complete water splitting reaction, which is generally limited by the slow kinetic process (Fig. 5a), the high-cost of sacrificial agents and the low oxygen evolution potential (2.23 *vs.* NHE).[93] Ag_3PO_4 has been widely investigated as a promising effective photocatalytic OER semiconductors of a negative VB (2.81 *vs.* NHE).[94] For example, the $MoSe_2/Ag_3PO_4$ heterostructure has been fabricated to promote electron transport and retard the photocorrosion of Ag_3PO_4.[95] In another instance, graphdiyne was used as a mediator and stabilizer in the Ag_3PO_4/graphdiyne/g-C_3N_4 system that achieved an OER of 753 μmol h^{-1} g^{-1}.[96] Xu *et al.* synthesized Ag_3PO_4/MXene hybrids for oxygen evolution from water directly in the absence of a sacrificial agent where the 2D MXene (Ti_3C_2) functioned as the co-catalyst.[97] Cui and co-workers assembled Ag_3PO_4 nanoparticles within 3D graphene aerogels (GAs).[94] The well-defined and interconnected pores within 3D GAs enabled a large adsorption ability for Ag^+ that greatly contributed to the highly distributed Ag_3PO_4 NPs. The well-dispersed Ag_3PO_4 NPs provided abundant reaction sites and significantly enhanced photocurrent density with a steady OER performance from a water splitting of 4860 μmol h^{-1} g^{-1} in comparison to that of the bulk Ag_3PO_4 electrode (3471 μmol h^{-1} g^{-1}). Yang *et al.* established KOH-assisted (CN-N*x*) surface modification of g-C_3N_4 to allow closer interfacial contact between Ag_3PO_4 and g-C_3N_4 than that without the KOH-assisted sample (CN).[98] Evidenced by the transient absorption spectra, electrons at the CB of the CN-N0.02 had prolonged lifetimes to transfer from the CB to the shallow trap state (τ_1 = 3.1 ps, τ_2 = 51.6 ps) than that of the CN. The efficient electron transfer led to an oxygen-generation performance of 115 μmol L^{-1} from the optimal sample under blue light LED irradiation. Guo *et al.* developed the $SrTiO_3/Ag_3PO_4$ composites for visible light OER.[99] As $SrTiO_3$ only possesses UV response, the photo-corrosion of Ag_3PO_4 could be relieved when visible light illumination is applied, Fig. 5b. In such a system, photo-excited holes on the VB of Ag_3PO_4 could directly rapidly migrate to the VB of $SrTiO_3$, realizing dual active sites towards the OER reaction.

3.3 Antibacterial activity

The photocatalytic antibacterial process on Ag-based semiconductors can be described in two different pathways. One is attack from the aggressive radicals such as $^{\bullet}O_2^-$, $^{\bullet}OH$ and $^1O_2$ that formed on semiconductors (Fig. 6a). Another is the released free Ag^+ directly attacking bacterial cell membrane and destroying cellular content to kill germs. The inherent antibiosis performance of Ag led to numerous antibacterial Ag based photocatalysts.

In situ growth of Ag_2S nanoparticles on the WS_2 nanosheets was reported by Wu and co-workers.[100] The similar metal–S bond of Ag_2S and WS_2 led to a tight hetero-interface. During photodynamic therapy application, Ag_2S could generate reactive oxygen species, *e.g.*, $^{\bullet}O_2^-$, $^1O_2$ or $^{\bullet}OH$, to effectively break the bacterial membrane. The prepared Ag_2S@WS_2 exhibited superior NIR light response with 99.93% inactivation of *Staphylococcus aureus* and 99.84% of *Escherichia coli* within 20 min under NIR light illumination. Wang *et al.* prepared Ag/Ag_2S/rGO with thiourea as the sulphur source through a hydrothermal reaction.[101] The coexistence of narrow bandgap Ag_2S and plasmonic Ag assisted the photo-induced electron–hole pairs separation and extended the light absorption to the wide spectrum region. In detail, the suitable VB of Ag_2S led to the effective reduction from H_2O to $^{\bullet}OH$, while Ag NPs efficiently removed electrons from CB of Ag_2S, facilitating the formation of $^{\bullet}O_2^-$. This led to an excellent photocatalytic degradation efficiency for ciprofloxacin (CIP) and outstanding antibacterial activity.

Wang *et al.* applied Ag/AgCl nanoparticles in photocatalytic anticancer performance where Ag nanoparticles served as both

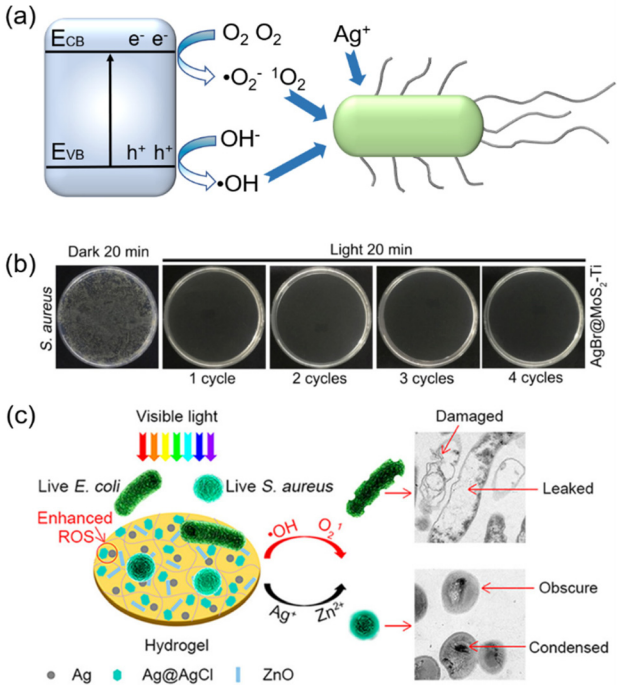

Fig. 6 (a) The scheme illustration of photocatalytic bacteriostasis. (b) The cyclic antibacterial performance of AgBr@MoS_2–Ti. (c) The disinfection mechanism towards *E. coli* and *S. aureus* of Ag/Ag@AgCl/ZnO. (b) Reproduced with permission from ref. 104 Copyright (2019) American Chemical Society. (c) Reproduced with permission from ref. 106 Copyright (2017) American Chemical Society.

photo-generated electrons trapper and hot carrier supplier.[102] Control experiments were implemented to explore the anticancer mechanism. More $^1O_2$ radicals were detected in Ag/10% AgCl compared with Ag NPs under light irradiation through the $^1O_2$ capture experiment, which indicated the favourable $^1O_2$ generation on AgCl. Meanwhile, this process was assisted by Ag NPs through facilitating charge separation. Graphitized hollow $ZnFe_2O_4$ nanospheres decorated by AgCl nanocubes and metallic Ag using polydopamine (PDA) as both template and reductant for Ag^+ were successfully fabricated by Zhang and co-workers.[103] The synergistic effect between Ag/AgCl and G-$ZnFe_2O_4$, and the distinctive hollow double-shell structure enabled the superior ability to inactivate *E. coli* and *S. aureus* that lasted for over 12 recycles. The excellent ability originated from the abundant photo-generated electrons delivered by Ag NPs and the correspondingly induced rapid $^{\bullet}O_2^-$/$^{\bullet}$OH formation. Wu *et al.* suggested the strong covalent binding between Ag and S due to the tight connection at the interface between AgBr and MoS_2.[104] A small shift of the S 2p peaks to the higher binding energy direction was observed, well demonstrating the interaction of the intensive electron field between MoS_2 and AgBr. Standing on the steady structure, photo-excited electrons transferred from MoS_2 to AgBr through the tight Ag–S bonds in an efficient manner, while O_2 was simultaneously reduced to $^1O_2$. The obtained AgBr@MoS_2–Ti sample maintained the antibacterial efficiency against *S. aureus* of 98.96% under 660 nm light irradiation for 20 min during a four-cycle measurement (Fig. 6b). In the $CeVO_4$/Ag nano-hybrid photocatalytic system, sulfhydryl was induced through the thiolene click reaction for stabilization and self-assembly of the Ag^+ ions. Subsequently reduced by Ce^{3+}, the final $CeVO_4$/Ag hybrid was effective in tumor suppression under vis/NIR light irradiation as a result of its excellent ability to generate $^{\bullet}O_2^-$ and $^{\bullet}$OH on Ag and the VB of $CeVO_4$, respectively.[105]

In addition to the free radicals mentioned above, Ag^+ can break the cell membrane of germs through the peptidoglycan reaction. Subsequently, the invasive Ag^+ will block adenosine triphosphate (ATP) production, interfere DNA replication and denature protein. It is of great challenge to release Ag^+ within a long period. As shown in Fig. 6c, the Ag/Ag@AgCl/ZnO system was embedded with the hydrogel by Wu *et al.*[106] On the one hand, the low photoenergy conversion efficiency of pure ZnO was overcome by participating Ag/Ag@AgCl heterostructures. On the other hand, the hydrogel environment benefited the Ag^+ and Zn^{2+} releasing with 90% Zn^{2+} released within 3 days under acidic conditions, while only 10% Zn^{2+} can be released after 21 days in a neutral environment. In addition, controllable sustained releases of the Ag^+ and Zn^{2+} were achieved through changing the pH value that enabled great potential in antibacterial and tissue repair applications. The polydopamine/Ag_3PO_4/graphene oxide (GO) hybrids were developed by Wu *et al.* for bacterial disinfection.[107] By tuning the proportion of GO, the bandgap of Ag_3PO_4/GO could be adjusted from 2.52 eV to 2.0 eV resulting in the visible light activity at the wavelength of 660 nm. Moreover, GO could modulate the Ag^+ releasing rate and accelerate electron transport due to its excellent electrical conductivity.

3.4 Pollutant removal

Pollutant degradation has been an emerging application in recent decades. The mechanism of pollutant removal was similar to photocatalytic bacteriostasis, where $^{\bullet}O_2^-$, $^{\bullet}$OH *etc.* are dominative radicals for degrading pollutants. For example, Liu *et al.* developed closely contacted p-type AgI and n-type $Bi_2Ga_4O_9$ through an intensive electrostatic adsorption approach.[108] The AgI/$Bi_2Ga_4O_9$ p–n heterojunction reached an $^{\bullet}O_2^-$ concentration 12.5 times higher than that of pure $Bi_2Ga_4O_9$ within 60 min, which can be attributed to the efficient charge separation and transfer at the p–n interfacial junction (Fig. 7a). More importantly, the formation of the superoxide radical was the rate determining step for pollutant decomposition, which was closely influenced by charge separation. The construction of a high efficiency charge transfer system was of great significance to improve removal performance. Reported by Zhao *et al.*, the Ag_2O/$BaTiO_3$ heterostructure promoted carrier separation due to the tuneable built-in field in $BaTiO_3$ which can be adjusted by ultrasonic excitation cycling and temperature field.[109] Ferroelectric nanocrystals of $BaTiO_3$ were combined with Ag_2O by Liu and co-workers.[110] The photo-induced electron/hole pairs in Ag_2O had different separation directions before polarization. Under ultrasonic

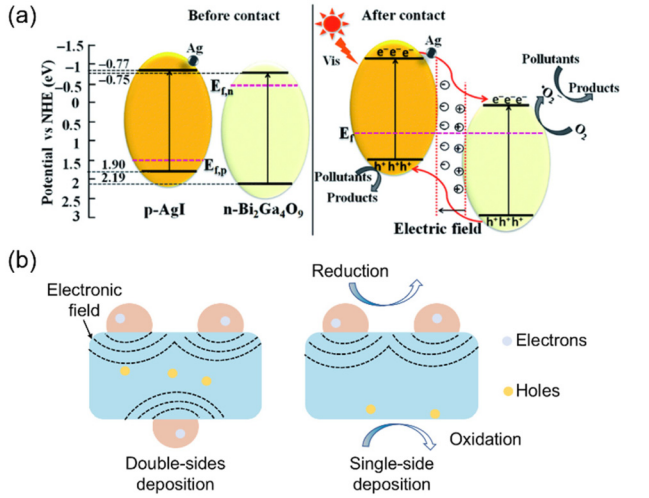

Fig. 7 (a) The AgI/$Bi_2Ga_4O_9$ p–n junction formation process and pollutant removal pathway. (b) The nonsymmetrical effect of Ag/AgI. (a) Reproduced with permission from ref. 108 Copyright (2020) Royal Society of Chemistry.

excitation, the polarization of $BaTiO_3$ induced a directed built-in electric field that drove electrons and holes on the C+ and C− sides of $BaTiO_3$, respectively, which greatly benefited the charge separation. As a representative p-type semiconductor, Ag_2O was also applied to develop a ZnO/Ag_2O p–n nano-heterojunction through a microwave-assisted synthesis.[111,112] The strong interaction between ZnO and Ag_2O at the interface and the narrow bandgap of Ag_2O enabled the alteration of the bandgap to 2.9 eV for the 5% Ag_2O–ZnO composite from the pure ZnO (3.2 eV) that provided driving forces for electron and hole separation/migration in a more efficient manner. Zaleska-Medynska *et al.* adopted a one-step anodic oxidation approach to synthesize self-organized TiO_2/Ag_2O NT arrays using Ti–Ag alloys in an electrolyte containing fluoride.[113] A small amount of Ag^+ was then electrochemically reduced to Ag NPs which were located inside NTs, or deposited on NTs or embedded into the wall. The coexistence of Ag_2O and Ag enabled the TiO_2/Ag_2O/Ag nanocomposites to harvest and utilize a far greater amount of incident photons standing on the LSPR effect of metallic Ag and narrow bandgap Ag_2O than that of the TiO_2 NT. The experimental results showed a great impact on the photocatalytic activity from the Ag^+/Ag content, demonstrating the governing role of the coexisted Ag^+ and metallic Ag.

Numerous excellent research studies were also reviewed. Zhou *et al.* modified self-floating porous black TiO_2 foams (FBTFs) with Ag nanoparticles through a two-step approach – wet-impregnation then high-temperature surface hydrogenation which resulted in significant enhancement on the photocatalytic activity of FBTFs.[52] The photocatalytic degradation efficiency reached 98% for thiobencarb in 2.5 h and remained almost constant after 10 recycles. In addition, the surface photovoltage spectra revealed that Ag-FBTFs had an obvious response peak of Ag at 475 nm owing to the strong SPR effect of Ag. Ag/P-g-C_3N_4 composites was prepared through a facile photo-reduction method by Xu *et al.*, and reached 100% degradation of SMX within 20 min that can also be attributed to the dual functional Ag.[114] Tian *et al.* prepared a Ag_2O NP/TiO_2 nanobelt heterostructure of a type I junction that significantly enhanced the charge separation efficiency during the degradation of methyl orange (MO) under UV, visible and NIR (near-infrared) irridation.[115] Fan *et al.* also fabricated a steady Ag_2O/B-g-C_3N_4 p–n junction utilizing bulk g-C_3N_4 (B-g-C_3N_4) of negative surface charge.[116] This structure presented excellent stability during photocatalytic degradation of rhodamine B with almost unchanged efficiency after 3 consecutive cycles for 15 h. Huang *et al.* demonstrated facet-dependent photocatalytic activity of the Ag_2O crystals with a series of morphologies including cubes, cuboctahedra, rhombicuboctahedra, octahedral, corner-truncated octahedra and rhombic dodecahedra which were synthesized through a simple precipitation preparation by adjusting the concentration of H_2O, NaOH, NH_4NO_3 and $AgNO_3$.[117] Among them, the Ag_2O cubes exhibited the most outstanding photocatalytic activity towards MO photodegradation. Superhydrophobic and superhydrophilic Ag_2O were synthesized by Jiang *et al.* for application in floating oil and organic dye degradation.[118] The wetting property of Ag_2O can be converted from hydrophilic to hydrophobic through a simple particle size increasing by ultrasonication, grinding or aging processes with no low-surface-energy modifiers required during practical applications.

Cheng and co-workers also synthesized the Ag–Ag_2O/reduced TiO_2 nanocomposites through a facile one-step wet-chemical reduction process in the presence of KBH_4.[119] The synergistic effect within Ag/Ag_2O and the Ag_2O/reduced TiO_2 type-II junction greatly elevated visible light activity, as evidenced by the diffuse reflectance spectra and diclofenac removal efficiency. Moreover, Yang *et al.* modified the TiO_2 with co-dopants of Ag and Ag_2O with nonmetal (P) and Ag_3PO_4,[120] which enabled a narrow bandgap value of 2.2 eV for the P/Ag/Ag_2O/Ag_3PO_4/TiO_2 composite. As the photo-excited electron trapped in the composite, Ag efficiently removed electrons from Ag_2O and Ag_3PO_4 facilitating the utilization efficiency of visible light. The resulting efficient charge separation led to an extremely stable hybrid structure and catalytic performance with a degradation rate of rhodamine B of 97.1% within 60 min. Fang *et al.* designed an innovative 2D nonsymmetrical heterostructure Ag/AgI nanoplate using a soft-template method.[121] The homogeneous coating of Ag made one side of AgI appear rough and another side considerably smooth. A superior degradation rate for Rh B on the nonsymmetrical Ag/AgI nanoplate with excellent stability in contrast to that of the symmetrical Au@AgI and Ag@AgI. As shown in Fig. 7b, such a novel asymmetric heterostructure would effectively relieve the binding effect that allows a larger proportion of holes to participate in the oxidation reaction.

Hu *et al.* modified Ag_3PO_4 with the carbon dots (CDs) and successfully tuned the band-edge position of Ag_3PO_4 for efficient degradation of dyes and pollutants.[122] CD decoration enabled all the samples to have more negative CB edge than

the redox potential of 4-NP/4-AP. The CDs@Ag_3PO_4 had an excellent conversion rate of transition from 4-NP to 4-AP with negligible drop during 5 recycles. This work proposed a feasible strategy for the energy band configuration of Ag_3PO_4 aiming at better performance and durability during photocatalytic application. Another C-based material, N doped carbon (NC), was firstly decorated on Ag_3PO_4 to establish the interfacial built-in electric field for rapid electron–hole pair separation.[123] The charge density calculation results demonstrated that the charges accumulated at the Ag_3PO_4 (100)@NC interface formed a built-in electric field pointing from NC to Ag_3PO_4. This greatly promoted charge transfer and led to a 100% degradation for norfloxacin, diclofenac, and phenol within 5, 8 and 12 min, respectively.

4. Prospective and conclusion

In summary, Ag based photocatalysts have demonstrated excellent tunability and great potential in emerging photocatalysis applications. This is particularly benefitting from the tuneable LSPR and moderate work function of Ag through the construction of a Schottky junction/ohmic contact within the metal–semiconductor hybrid system. The present review discussed the fundamental mechanisms behind the LSPR effect, Schottky junction and ohmic contact, as well as urgent issues in Ag based photocatalysts including: the low alcohol and hydrocarbon selectivity in CO_2 reduction, low oxygen evolution rate in water splitting, difficulty in the control of Ag^+ release rate and inefficient charge separation in pollutant degradation. The photocatalytic performance of Ag based photocatalysis still leaves vast development space and a great opportunity to reach the ideal state. Based on the review, we propose the following modification strategies in the area as follows:

(1) The LSPR effect of Ag can be adjusted by morphology and size. So far, the morphological effect has been deeply developed, yet the size effects from single atoms, clusters and nanoparticles as well as their coordination have been rarely reached. Especially in the cluster category, tens of Ag atoms possess a discrete band structure and thus can be excited by light with different wavelengths. Precisely tailoring the Ag cluster on the atomic scale and the arrangement would enable a finely tuned band structure and LSPR effect towards further development of their photocatalysis application.

(2) Single metals have drawbacks such as a limited ability to match band structures of all semiconductors, while bimetallic and even trimetallic systems have the potential to align well with the band structure of specific semiconductors. The Fermi level of the Ag based multi-metal system can be regulated on a large scale through cooperating with different kinds of metals and contents, which would allow a sophisticated design in the band bending, barrier height and charge transform of the constructed Schottky junction/ohmic contacts towards more specific applications. On the other hand, an Ag based multi-metal system would enable sufficient CO* adsorption and thus lead to higher alcohol and hydrocarbon selectivity than the single Ag metal based photocatalysis system.

Author contributions

The manuscript was written through the contributions of all authors. YZ carried out the preparation of the draft. JL, YSK and XLZ contributed through discussion, manuscript preparation and amending. All authors have given approval to the final version of the manuscript.

Conflicts of interest

All authors declare that they have no conflict of interest.

Acknowledgements

XLZ acknowledges the National Natural Science Foundation of China (NSFC, 51602291).

References

1 J. Kosco, M. Bidwell, H. Cha, T. Martin, C. T. Howells, M. Sachs, D. H. Anjum, S. Gonzalez Lopez, L. Zou, A. Wadsworth, W. Zhang, L. Zhang, J. Tellam, R. Sougrat, F. Laquai, D. M. DeLongchamp, J. R. Durrant and I. McCulloch, *Nat. Mater.*, 2020, **19**, 559–565.
2 H. Nishiyama, T. Yamada, M. Nakabayashi, Y. Maehara, M. Yamaguchi, Y. Kuromiya, Y. Nagatsuma, H. Tokudome, S. Akiyama, T. Watanabe, R. Narushima, S. Okunaka, N. Shibata, T. Takata, T. Hisatomi and K. Domen, *Nature*, 2021, **598**, 304–307.
3 N. Feng, H. Lin, H. Song, L. Yang, D. Tang, F. Deng and J. Ye, *Nat. Commun.*, 2021, **12**, 4652.
4 X. Zheng, L. Feng, Y. Dou, H. Guo, Y. Liang, G. Li, J. He, P. Liu and J. He, *ACS Nano*, 2021, **15**, 13209–13219.
5 M. Cai, Z. Wu, Z. Li, L. Wang, W. Sun, A. A. Tountas, C. Li, S. Wang, K. Feng, A.-B. Xu, S. Tang, A. Tavasoli, M. Peng, W. Liu, A. S. Helmy, L. He, G. A. Ozin and X. Zhang, *Nat. Energy*, 2021, **6**, 807–814.
6 J. Jing, J. Yang, W. Li, Z. Wu and Y. Zhu, *Adv. Mater.*, 2021, e2106807.
7 H. Hu, Z. Wang, L. Cao, L. Zeng, C. Zhang, W. Lin and C. Wang, *Nat. Chem.*, 2021, **13**, 358–366.
8 W. Zhang, H. He, H. Li, L. Duan, L. Zu, Y. Zhai, W. Li, L. Wang, H. Fu and D. Zhao, *Adv. Energy Mater.*, 2020, **11**, 2003303.
9 X. Shen, J. Yang, T. Zheng, Q. Wang, H. Zhuang, R. Zheng, S. Shan and S. Li, *Sep. Purif. Technol.*, 2020, **251**, 117347.
10 E. Cortes, *Science*, 2018, **362**, 28–29.
11 C. Zhang, H. Hua, J. Liu, X. Han, Q. Liu, Z. Wei, C. Shao and C. Hu, *Nano-Micro Lett.*, 2017, **9**, 49.

12 T. Kawawaki, T. Nakagawa, M. Sakamoto and T. Teranishi, *J. Am. Chem. Soc.*, 2019, **141**, 8402–8406.
13 T. Takata, J. Jiang, Y. Sakata, M. Nakabayashi, N. Shibata, V. Nandal, K. Seki, T. Hisatomi and K. Domen, *Nature*, 2020, **581**, 411–414.
14 C. Zhang, F. Zhou, S. Zhan, Y. Song, F. Wang and J. Lai, *Environ. Res.*, 2021, **197**, 111129.
15 Y. Lei, S. Xu, M. Ding, L. Li, Q. Sun and Z. L. Wang, *Adv. Funct. Mater.*, 2020, **30**, 2005716.
16 H. Zhang, T. Itoi, T. Konishi and Y. Izumi, *J. Am. Chem. Soc.*, 2019, **141**, 6292–6301.
17 M. J. Landry, A. Gellé, B. Y. Meng, C. J. Barrett and A. Moores, *ACS Catal.*, 2017, **7**, 6128–6133.
18 F. Widdascheck, A. A. Hauke and G. Witte, *Adv. Funct. Mater.*, 2019, **29**, 1808385.
19 L. Zhang, M. Can, S. W. Ragsdale and F. A. Armstrong, *ACS Catal.*, 2018, **8**, 2789–2795.
20 T. H. Jeon, D. Monllor-Satoca, G. H. Moon, W. Kim, H. I. Kim, D. W. Bahnemann, H. Park and W. Choi, *Nat. Commun.*, 2020, **11**, 967.
21 C. Cao, H. Zou, N. Yang, H. Li, Y. Cai, X. Song, J. Shao, P. Chen, X. Mou, W. Wang and X. Dong, *Adv. Mater.*, 2021, e2106996.
22 R. K. Sharma, S. Yadav, S. Dutta, H. B. Kale, I. R. Warkad, R. Zboril, R. S. Varma and M. B. Gawande, *Chem. Soc. Rev.*, 2021, **50**, 11293–11380.
23 Y. Du, H. Sheng, D. Astruc and M. Zhu, *Chem. Rev.*, 2020, **120**, 526–622.
24 H. Kang, J. T. Buchman, R. S. Rodriguez, H. L. Ring, J. He, K. C. Bantz and C. L. Haynes, *Chem. Rev.*, 2019, **119**, 664–699.
25 X. Li, J. Yu, M. Jaroniec and X. Chen, *Chem. Rev.*, 2019, **119**, 3962–4179.
26 A. N. Koya, X. Zhu, N. Ohannesian, A. A. Yanik, A. Alabastri, R. Proietti Zaccaria, R. Krahne, W. C. Shih and D. Garoli, *ACS Nano*, 2021, **15**, 6038–6060.
27 C. Liang, Z. A. Lu, J. Wu, M. X. Chen, Y. Zhang, B. Zhang, G. L. Gao, S. Li and P. Xu, *ACS Appl. Mater. Interfaces*, 2020, **12**, 54266–54284.
28 S. Rtimi, D. D. Dionysiou, S. C. Pillai and J. Kiwi, *Appl. Catal., B*, 2019, **240**, 291–318.
29 Y. Shi, J. Ma, Y. Chen, Y. Qian, B. Xu, W. Chu and D. An, *Sci. Total Environ.*, 2021, **804**, 150024.
30 W. Xue, D. Huang, X. Wen, S. Chen, M. Cheng, R. Deng, B. Li, Y. Yang and X. Liu, *J. Hazard. Mater.*, 2020, **390**, 122128.
31 Q. Yao, X. Yuan, T. Chen, D. T. Leong and J. Xie, *Adv. Mater.*, 2018, **30**, e1802751.
32 R. W. Wood, *Proc. Phys. Soc., London*, 1902, **18**, 269–275.
33 X. Liu, M. Ye, S. Zhang, G. Huang, C. Li, J. Yu, P. K. Wong and S. Liu, *J. Mater. Chem. A*, 2018, **6**, 24245–24255.
34 N. Zhang, M. Li, C. F. Tan, C. K. Nuo Peh, T. C. Sum and G. W. Ho, *J. Mater. Chem. A*, 2017, **5**, 21570–21578.
35 X. Y. Xu, F. T. Luo, W. S. Tang, J. G. Hu, H. B. Zeng and Y. Zhou, *Adv. Funct. Mater.*, 2018, **28**, 1804055.
36 Z. Li and D. Kurouski, *Acc. Chem. Res.*, 2021, **54**, 2477–2487.
37 N. Jiang, X. Zhuo and J. Wang, *Chem. Rev.*, 2018, **118**, 3054–3099.
38 A. Gelle, T. Jin, L. de la Garza, G. D. Price, L. V. Besteiro and A. Moores, *Chem. Rev.*, 2020, **120**, 986–1041.
39 J. E. Lee, S. Bera, Y. S. Choi and W. I. Lee, *Appl. Catal., B*, 2017, **214**, 15–22.
40 S. Linic, P. Christopher and D. B. Ingram, *Nat. Mater.*, 2011, **10**, 911–921.
41 M. Song, A. Bouhelier, P. Bramant, J. Sharma, E. Dujardin, D. Zhang and G. Colas-des-Francs, *ACS Nano*, 2011, **5**, 5874–5880.
42 X. Gao, R. J. Esteves, T. T. Luong, R. Jaini and I. U. Arachchige, *J. Am. Chem. Soc.*, 2014, **136**, 7993–8002.
43 M. M. Shahjamali, Y. Zhou, N. Zaraee, C. Xue, J. Wu, N. Large, C. M. McGuirk, F. Boey, V. Dravid, Z. Cui, G. C. Schatz and C. A. Mirkin, *ACS Nano*, 2016, **10**, 5362–5373.
44 F. Han, Z. Guan, T. S. Tan and Q. H. Xu, *ACS Appl. Mater. Interfaces*, 2012, **4**, 4746–4751.
45 K. Sugawa, H. Tahara, A. Yamashita, J. Otsuki, T. Sagara, T. Harumoto and S. Yanagida, *ACS Nano*, 2015, **9**, 1895–1904.
46 V. P. Sandireddy, K. P. Koirala, H. Taz and R. Kalyanaraman, *ACS Appl. Mater. Interfaces*, 2018, **10**, 33630–33639.
47 D. Schletz, J. Schultz, P. L. Potapov, A. M. Steiner, J. Krehl, T. A. F. Konig, M. Mayer, A. Lubk and A. Fery, *Adv. Opt. Mater.*, 2021, **9**, 2001983.
48 N. Macia, R. Bresoli-Obach, S. Nonell and B. Heyne, *J. Am. Chem. Soc.*, 2019, **141**, 684–692.
49 X. Zhang, X. Wang, H. Cheng, Y. Zheng, J. Zhao and K. Qu, *J. Hazard. Mater.*, 2021, **413**, 125320.
50 Z. B. Zhan, F. Grote, Z. J. Wang, R. Xu and Y. Lei, *Adv. Energy Mater.*, 2015, **5**, 1501654.
51 Y. Negrín-Montecelo, M. Comesaña-Hermo, L. K. Khorashad, A. Sousa-Castillo, Z. Wang, M. Pérez-Lorenzo, T. Liedl, A. O. Govorov and M. A. Correa-Duarte, *ACS Energy Lett.*, 2019, **5**, 395–402.
52 H. Li, L. Shen, K. Zhang, B. Sun, L. Ren, P. Qiao, K. Pan, L. Wang and W. Zhou, *Appl. Catal., B*, 2018, **220**, 111–117.
53 J. Cai, J. Huang, S. Wang, J. Iocozzia, Z. Sun, J. Sun, Y. Yang, Y. Lai and Z. Lin, *Adv. Mater.*, 2019, **31**, e1806314.
54 H. Jiang, Z. P. Xing, T. Y. Zhao, Z. K. Yang, K. Wang, Z. Z. Li, S. L. Yang, L. Y. Xie and W. Zhou, *Appl. Catal., B*, 2020, **274**, 118947.
55 L. Wang, D. Lv, Z. Yue, H. Zhu, L. Wang, D. Wang, X. Xu, W. Hao, S. X. Dou and Y. Du, *Nano Energy*, 2019, **57**, 398–404.
56 Y. Duan, M. Zhang, L. Wang, F. Wang, L. Yang, X. Li and C. Wang, *Appl. Catal., B*, 2017, **204**, 67–77.
57 X. Huang, H. Li, C. Zhang, S. Tan, Z. Chen, L. Chen, Z. Lu, X. Wang and M. Xiao, *Nat. Commun.*, 2019, **10**, 1163.
58 J. Ding, Y. Bu, M. Ou, Y. Yu, Q. Zhong and M. Fan, *Appl. Catal., B*, 2017, **202**, 314–325.

59 Q. Lang, Y. Chen, T. Huang, L. Yang, S. Zhong, L. Wu, J. Chen and S. Bai, *Appl. Catal., B*, 2018, **220**, 182–190.
60 X. Zhang, G. Kumari, J. Heo and P. K. Jain, *Nat. Commun.*, 2018, **9**, 3056.
61 L. C. Sim, K. H. Leong, S. Ibrahim and P. Saravanan, *J. Mater. Chem. A*, 2014, **2**, 5315–5322.
62 V. Kumaravel, S. Mathew, J. Bartlett and S. C. Pillai, *Appl. Catal., B*, 2019, **244**, 1021–1064.
63 R. S. Haider, S. Wang, Y. Gao, A. S. Malik, N. Ta, H. Li, B. Zeng, M. Dupuis, F. Fan and C. Li, *Nano Energy*, 2021, **87**, 106189.
64 L. J. Krayer, K. J. Palm, C. Gong, A. Torres, C. E. P. Villegas, A. R. Rocha, M. S. Leite and J. N. Munday, *ACS Photonics*, 2020, **7**, 1689–1698.
65 S. Wu, X. Shen, G. Zhu, H. Zhou, Z. Ji, K. Chen and A. Yuan, *Appl. Catal., B*, 2016, **184**, 328–336.
66 J. Chen, H. Che, K. Huang, C. Liu and W. Shi, *Appl. Catal., B*, 2016, **192**, 134–144.
67 D. Tsukamoto, A. Shiro, Y. Shiraishi, Y. Sugano, S. Ichikawa, S. Tanaka and T. Hirai, *ACS Catal.*, 2012, **2**, 599–603.
68 F. Yan, Y. Wu, L. Jiang, X. Xue, J. Lv, L. Lin, Y. Yu, J. Zhang, F. Yang and Y. Qiu, *ChemSusChem*, 2020, **13**, 876–881.
69 H. Liu, X. Liu, W. Yang, M. Shen, S. Geng, C. Yu, B. Shen and Y. Yu, *J. Mater. Chem. A*, 2019, **7**, 2022–2026.
70 Q. Liu, Z. Wang, H. Chen, H. Y. Wang, H. Song, J. Ye and Y. Weng, *ChemCatChem*, 2020, **12**, 3838–3842.
71 F. Yan, Y. Wang, J. Zhang, Z. Lin, J. Zheng and F. Huang, *ChemSusChem*, 2014, **7**, 101–104.
72 S. Bai, X. Li, Q. Kong, R. Long, C. Wang, J. Jiang and Y. Xiong, *Adv. Mater.*, 2015, **27**, 3444–3452.
73 D. Devasia, A. J. Wilson, J. Heo, V. Mohan and P. K. Jain, *Nat. Commun.*, 2021, **12**, 2612.
74 T. Ishii, A. Anzai, A. Yamamoto and H. Yoshida, *Appl. Catal., B*, 2020, **277**, 119192.
75 Z. Li, Y. Yang, J. Tian, J. Li, G. Chen, L. Zhou, Y. Sun and Y. Qiu, *ChemSusChem*, 2022, **15**, e202102729.
76 B. Hammer, Y. Morikawa and J. K. Norskov, *Phys. Rev. Lett.*, 1996, **76**, 2141–2144.
77 T. Zhang, H. Shang, B. Zhang, D. Yan and X. Xiang, *ACS Appl. Mater. Interfaces*, 2021, **13**, 16536–16544.
78 Y. Sun, G. Li, Y. Gong, Z. Sun, H. Yao and X. Zhou, *J. Hazard. Mater.*, 2021, **403**, 124019.
79 D. Hong, L.-M. Lyu, K. Koga, Y. Shimoyama and Y. Kon, *ACS Sustainable Chem. Eng.*, 2019, **7**, 18955–18964.
80 Z. L. Tang, W. J. He, Y. L. Wang, Y. C. Wei, X. L. Yu, J. Xiong, X. Wang, X. Zhang, Z. Zhao and J. Liu, *Appl. Catal., B*, 2022, **311**, 121371.
81 H. Li, S. Gan, H. Wang, D. Han and L. Niu, *Adv. Mater.*, 2015, **27**, 6906–6913.
82 D. Tan, J. Zhang, J. Shi, S. Li, B. Zhang, X. Tan, F. Zhang, L. Liu, D. Shao and B. Han, *ACS Appl. Mater. Interfaces*, 2018, **10**, 24516–24522.
83 M. Yamamoto, T. Yoshida, N. Yamamoto, T. Nomoto, Y. Yamamoto, S. Yagi and H. Yoshida, *J. Mater. Chem. A*, 2015, **3**, 16810–16816.
84 Y. Xiong, H. Chen, Y. Hu, S. Yang, X. Xue, L. He, X. Liu, J. Ma and Z. Jin, *Nano Lett.*, 2021, **21**, 8693–8700.
85 Y. Wang, X. H. Liu, Q. Wang, M. Quick, S. A. Kovalenko, Q. Y. Chen, N. Koch and N. Pinna, *Angew. Chem., Int. Ed.*, 2020, **59**, 7748–7754.
86 P. Verma, K. Yuan, Y. Kuwahara, K. Mori and H. Yamashita, *Appl. Catal., B*, 2018, **223**, 10–15.
87 Y. Yang, G. Zhuang, L. Sun, X. Zhang, X. Yan, W. Zhan, X. Wang and X. Han, *J. Mater. Chem. A*, 2020, **8**, 17449–17453.
88 W. L. Ong, Y.-F. Lim, J. L. Ting Ong and G. W. Ho, *J. Mater. Chem. A*, 2015, **3**, 6509–6516.
89 X. C. Zhang, T. Y. Liu, F. Zhao, N. Zhang and Y. H. Wang, *Appl. Catal., B*, 2021, **298**, 120620.
90 Z. Z. Lou, S. Kim, M. Fujitsuka, X. G. Yang, B. J. Li and T. Majima, *Adv. Funct. Mater.*, 2018, **28**, 1706969.
91 T. Bora and J. Dutta, *J. Nanosci. Nanotechnol.*, 2019, **19**, 383–388.
92 H. An, M. Li, R. Liu, Z. Gao and Z. Yin, *Chem. Eng. J.*, 2020, **382**, 122953.
93 S. C. Sun, G. Q. Shen, J. W. Jiang, W. B. Mi, X. L. Liu, L. Pan, X. W. Zhang and J. J. Zou, *Adv. Energy Mater.*, 2019, **9**, 1901505.
94 C. Cui, S. Li, Y. Qiu, H. Hu, X. Li, C. Li, J. Gao and W. Tang, *Appl. Catal., B*, 2017, **200**, 666–672.
95 D. Li, H. Wang, H. Tang, X. Yang and Q. Liu, *ACS Sustainable Chem. Eng.*, 2019, **7**, 8466–8474.
96 H.-Y. Si, C.-J. Mao, J.-Y. Zhou, X.-F. Rong, Q.-X. Deng, S.-L. Chen, J.-J. Zhao, X.-G. Sun, Y. M. Shen, W.-J. Feng, P. Gao and J. Zhang, *Carbon*, 2018, **132**, 598–605.
97 C. X. Zhao, X. F. Yang, C. H. Han and J. S. Xu, *Sol. RRL*, 2020, **4**, 1900434.
98 C. X. Zhao, L. Tian, Z. Y. Zou, Z. P. Chen, H. Tang, Q. Q. Liu, Z. X. Lin and X. F. Yang, *Appl. Catal., B*, 2020, **268**, 118445.
99 X. Guan and L. Guo, *ACS Catal.*, 2014, **4**, 3020–3026.
100 Y. Lin, D. Han, Y. Li, L. Tan, X. Liu, Z. Cui, X. Yang, Z. Li, Y. Liang, S. Zhu and S. Wu, *ACS Sustainable Chem. Eng.*, 2019, **7**, 14982–14990.
101 P. Huo, C. Liu, D. Wu, J. Guan, J. Li, H. Wang, Q. Tang, X. Li, Y. Yan and S. Yuan, *J. Ind. Eng. Chem.*, 2018, **57**, 125–133.
102 X. Zhang, P. Wang, W. Meng, E. Cui, Q. Zhang, Z. Wang, Z. Zheng, Y. Liu, H. Cheng, Y. Dai and B. Huang, *Chem. Eng. J.*, 2022, **428**, 131265.
103 C. Zhang, Y. Gu, G. Teng, L. Wang, X. Jin, Z. Qiang and W. Ma, *ACS Appl. Mater. Interfaces*, 2020, **12**, 29883–29898.
104 W. Zhu, X. Liu, L. Tan, Z. Cui, X. Yang, Y. Liang, Z. Li, S. Zhu, K. W. K. Yeung and S. Wu, *ACS Appl. Mater. Interfaces*, 2019, **11**, 34364–34375.
105 M. Chang, M. Wang, Y. Chen, M. Shu, Y. Zhao, B. Ding, Z. Hou and J. Lin, *Nanoscale*, 2019, **11**, 10129–10136.
106 C. Mao, Y. Xiang, X. Liu, Z. Cui, X. Yang, K. W. K. Yeung, H. Pan, X. Wang, P. K. Chu and S. Wu, *ACS Nano*, 2017, **11**, 9010–9021.

107 X. Xie, C. Mao, X. Liu, L. Tan, Z. Cui, X. Yang, S. Zhu, Z. Li, X. Yuan, Y. Zheng, K. W. K. Yeung, P. K. Chu and S. Wu, *ACS Cent. Sci.*, 2018, **4**, 724–738.
108 J. Liu, X. Zhang, Q. Zhong, J. Li, H. Wu, B. Zhang, L. Jin, H. B. Tao and B. Liu, *J. Mater. Chem. A*, 2020, **8**, 4083–4090.
109 W. Zhao, Q. Zhang, H. G. Wang, J. C. Rong, E. Lei and Y. J. Dai, *Nano Energy*, 2020, **73**, 104783.
110 H. Li, Y. Sang, S. Chang, X. Huang, Y. Zhang, R. Yang, H. Jiang, H. Liu and Z. L. Wang, *Nano Lett.*, 2015, **15**, 2372–2379.
111 U. Chakraborty, G. Bhanjana, Kannu, N. Kaur, R. Sharma, G. Kaur, A. Kaushik and G. R. Chaudhary, *J. Hazard. Mater.*, 2021, **416**, 125771.
112 S. Ma, J. Xue, Y. Zhou and Z. Zhang, *J. Mater. Chem. A*, 2014, **2**, 7272–7280.
113 P. Mazierski, A. Malankowska, M. Kobylanski, M. Diak, M. Kozak, M. J. Winiarski, T. Klimczuk, W. Lisowski, G. Nowaczyk and A. Zaleska-Medynska, *ACS Catal.*, 2017, **7**, 2753–2764.
114 M. Chen, C. Guo, S. Hou, L. Wu, J. Lv, C. Hu, Y. Zhang and J. Xu, *J. Hazard. Mater.*, 2019, **366**, 219–228.
115 N. Wei, H. Cui, Q. Song, L. Zhang, X. Song, K. Wang, Y. Zhang, J. Li, J. Wen and J. Tian, *Appl. Catal., B*, 2016, **198**, 83–90.
116 G. D. Fan, B. H. Du, J. J. Zhou, W. W. Yu, Z. Y. Chen and S. W. Yang, *Appl. Catal., B*, 2020, **265**, 118610.
117 Y. J. Chen, Y. W. Chiang and M. H. Huang, *ACS Appl. Mater. Interfaces*, 2016, **8**, 19672–19679.
118 W. Jiang, H. Fu, Y. Zhu, H. Yue, S. Yuan and B. Liang, *Nanoscale*, 2018, **10**, 13661–13672.
119 Y. Cui, Q. Ma, X. Deng, Q. Meng, X. Cheng, M. Xie, X. Li, Q. Cheng and H. Liu, *Appl. Catal., B*, 2017, **206**, 136–145.
120 X. Hu, Q. Zhu, X. Wang, N. Kawazoe and Y. Yang, *J. Mater. Chem. A*, 2015, **3**, 17858–17865.
121 M. U. Khan, H. You, X. Liu, L. Zhang and J. Fang, *Small*, 2018, **4**, 1702948.
122 S. Hu, W. Yang, N. Li, H. Wang, J. Yang and Q. Chang, *Small*, 2018, **14**, e1803447.
123 Y. Lin, C. P. Yang, S. H. Wu, X. Li, Y. J. Chen and W. L. Yang, *Adv. Funct. Mater.*, 2020, **30**, 2002918.